ACS OMEGA

http://pubs.acs.org/journal/acsodf

Article

Plasmonic Metal/Semiconductor Heterostructure for Visible Light-Enhanced H_2 Production

Shomaila Khanam and Sanjeeb Kumar Rout*

Cite This: *ACS Omega* 2022, 7, 25466−25475

Read Online

ACCESS | Metrics & More | Article Recommendations | Supporting Information

ABSTRACT: A plasmonic Ag/Bi_2WO_6 heterostructure, having Ag NPs deposited on Bi_2WO_6, is obtained by a hydrothermal and photodeposition method. The synthesized Ag/Bi_2WO_6 composite exhibits strong visible light absorption with a localized surface plasmon resonance (LSPR) and shows an enhanced photoabsorption property. It is demonstrated that such a Ag/Bi_2WO_6 heterostructure shows excellent plasmon-enhanced photocatalytic activity in the dehydrogenation of ammonia borane (NH_3BH_3) solution under visible light irradiation, which is due to the results from the synergetic effect between Ag NPs and emerging W^{5+} ions. More importantly, the performance of a Ag/Bi_2WO_6 hybrid is almost eight times higher than that of sole Bi_2WO_6 nanosheets. The introduction of LSPR of Ag in Bi_2WO_6 improves the electrical conductivity of the composite and lowers the recombination rate of charge carriers. This study opens up the opportunity of rationally fabricating plasmonic metal/semiconductor heterostructures for highly efficient photocatalysis.

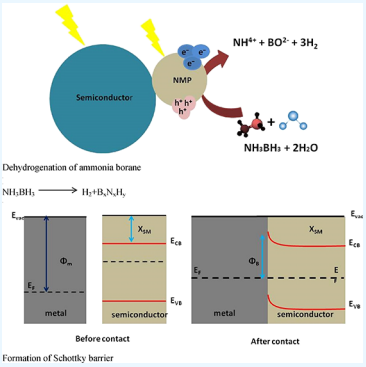

1. INTRODUCTION

Conversion of solar energy to hydrogen fuel from hydrogen storage materials through photocatalysis is accepted to be an excellent technique to harvest energy and to solve worldwide environmental issues.[1,2] Photocatalytic hydrolysis from hydrogen-rich compounds involves a semiconductor material as a photocatalyst, such as TiO_2, and a solar light source for hydrogen evolution.[3,4] Alternatively, the localized surface plasmon resonance (LSPR) of metals such as Au, Ag, and Pd along with a semiconductor has proven to be a significant candidate for photocatalysis.[5] Plasmonic nanostructures develop oscillation of electrons when they are incident by the light wave of plasmonic resonance frequency, which produces a bound or localized electromagnetic mode in a confined plasmonic nanostructure. This creates an enhanced electric field that produces energetic electrons and heat, which has been reported to be significant in the conversion of solar light energy to activate chemical reactions.[6] LSPR has proved to be highly effective in heterogeneous photocatalysis, and a single-component photocatalyst has low catalytic efficiency and cannot fulfill the desired requirements. Recently, a number of research studies on noble metal/semiconductor hybrid photocatalysts have been done, and they have proven successful in many reactions such as degradation, hydrogen evolution, hydrogenation, and oxidation.[7,8] The noble metal/semiconductor hybrid has found a strong place in the field of photocatalysis. Loading of a noble metal on a photocatalyst can result in an extended light response and enhances the interfacial charge transfer efficiency.[7−11] This enhanced local electric field leads to the increased interband transition rate, making the energy generated by LSPR higher than the bandgap of a semiconductor and increasing the electron−hole pair separation in the photocatalyst.[12−15] The electrons are directed toward a noble metal, and holes are accumulated on the other edge of a semiconductor. The noble metal acts as an electron trapper and reduces the recombination rate of electron−hole pairs. This process enhances the photoactivity of the photocatalyst. In contrast, too much noble metal reduces the active sites for the reaction and acts as a recombination center. The high concentration of noble metals blocks the active sites of the reaction. Figure S1 in the Supporting Information shows that the noble metal on the semiconductor absorbs the incident light and undergoes surface plasmon oscillation, which excites electrons and holes. However, the plasmonic enhancement of photoconversion is still a great challenge. To attain progress in this method, some basic problems, such as the fabrication size, geometry, and combination (molar ratio) of the noble metal and semiconductor, need to be thoroughly investigated. The energy transfer between plasmonic metals and semiconductors takes place through three mechanisms: light scattering, hot electron injection, and plasmon-induced resonance energy transfer.[16−18] Designing a plasmonic metal/semiconductor photocatalyst is a big challenge. However, some reported work shows that strongly coupled metal/semiconductor nanostructures generated a high intensity of

Received: April 20, 2022
Accepted: June 29, 2022
Published: July 14, 2022

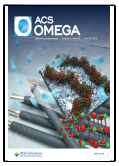

LSPR, but the kind of architecture of the metal/semiconductor heterostructure is still a mystery.[19−21]

There are studies available that have worked on the metal and semiconductor combination. Yu et al., in their work, have shown the LSPR effect of Au-chain@$Zn_xCd_{1-x}S$ and reported 54.6% of H_2 production.[22] Simagina and his team have also reported 330 μmol of hydrogen evolution from ammonia borane in 3 h over Ag/TiO_2.[23] Zhang et al. reported 3 mL/min H_2 production from NH_3BH_3 in 60 min over PtNi-graphite.[24] Hydrogen production of 1.1 mL/min from NH_3BH_3 (AB) has also been reported in $Pt@SiO_2$ heterostructures.[25] Table 1 summarizes the hydrogen evolution from ammonia borane over some reported plasmonic photocatalysts. Many noble metals, such as Ru, Rh, Au, and Pd, have resulted in high hydrogen yield from AB solution.[6,26] Silver nanoparticles, being cost-effective, will easily cut off the expenses of the photocatalyst. Herein, we report a green chemistry route to synthesize a plasmonic Ag/Bi_2WO_6 nanostructure by coupling a Bi_2WO_6 semiconductor and silver metal nanoparticles (NPs). More importantly, such a Ag/Bi_2WO_6 hybrid displayed a dramatic plasmon-enhanced photocatalytic activity in the photocatalytic hydrolysis of NH_3BH_3 solution under visible light irradiation.

Table 1. Hydrogen Evolution from Ammonia Borane over Some Reported Photocatalysts

catalyst	preparation method	time (min)	hydrogen evolution	reference
Bi_2WO_6	hydrothermal	150	0.050 μmol/min	present work
Ag/Bi_2WO_6 (1:1)	hydrothermal and photodeposition	150	0.13 μmol/min	present work
Ag/Bi_2WO_6 (1:2)	hydrothermal and photodeposition	150	6.608 μmol/min	present work
Ag/Bi_2WO_6 (2:1)	hydrothermal and photodeposition	150	0.57 μmol/min	present work
MoO_3	solvothermal	50	63.3 mol %	27
WO_3	solvothermal	50	10 mol %	27
Cu/TiO_2	sol−gel	60	90 mol %	28
Pt/TiO_2-ZnO	sol−gel	300	88 mol %	29
CdS-TiO_2	electrospinning	60	95 mol %	30
TiO_2 (nanofiber)	electrospinning	60	34 mol %	30
Au chain@ $Zn_xCd_{1-x}S$	hydrothermal	60	54.6 mol %	22
Ag/TiO_2	hydrothermal	180	330 μmol	23
PtNi-graphite	impregnation and chemical reduction	60	3 mL/min	24
$Pt@SiO_2$	sol−gel and chemical route	60	1.1 mL/min	25
TiO_2 (carbon nanofiber)	electrospinning	60	55 mol %	30

2. EXPERIMENTAL SECTION

2.1. Synthesis of Bi_2WO_6. $Na_2WO_4{\cdot}2H_2O$ (1.23 g) and $Bi(NO_3)_3{\cdot}5H_2O$ (3.64 g) were added to a Teflon jar containing 150 mL of deionized water under magnetic stirring in a conventional hydrothermal operation. The Teflon tank was sealed in an autoclave and heated for 20 h at 160 °C. The autoclave was allowed to cool naturally to ambient temperature after the reaction period was completed; the sample was centrifuged and washed multiple times with deionized water before being dried in an oven at 80 °C for 10 h. Finally, a yellowish Bi_2WO_6 nanopowder was synthesized.

2.2. Synthesis of Plasmonic Ag/Bi_2WO_6. The introduction of Ag on the semiconductor was achieved using photoinduced deposition of Ag on Bi_2WO_6. In a typical synthesis, 0.085 g (0.5 mmol) of $AgNO_3$ was added to a beaker containing 50 mL of deionized water and agitated continuously in the dark for 30 min. The $AgNO_3$ solution was then poured to 0.349 g (0.5 mmol) of hydrothermally generated Bi_2WO_6 and held in a visible light chamber for 60 min. A gray precipitate was obtained, which was rinsed multiple times with deionized water before being dried for 8 h at 60 °C in an oven. By varying the molar ratios of silver and bismuth tungstate, three distinct Ag/Bi_2WO_6 molar ratios (1:1, 1:2, and 2:1) were created. The synthesis of Ag/Bi_2WO_6 is depicted graphically in Figure S2.

2.3. Characterization. X-ray diffraction (XRD) patterns were used to verify the phase purity of the produced photocatalysts using a SmartLab diffractometer (Rigaku, Japan). The patterns were captured in the 2θ range of 10−70° using Cu Kα radiation (λ = 1.5416 Å), and the scanning rate was kept at 3° m^{-1}. FTIR and Raman spectroscopy were used to further investigate the detailed structural analyses. An IR-Prestige 21 spectrometer (Shimadzu Corp., Japan) was used to record the FTIR spectra in the frequency range of 400 to 4000 cm^{-1} using KBr as a diluting agent. A FESEM (Carl Zeiss Microscopy Ltd., Germany) apparatus equipped with an energy dispersive X-ray spectroscope was used to capture morphological images. Using a commercial (Quantachrome Instruments, USA) apparatus, the Brunauer−Emmett−Teller (BET) test was performed to determine the surface area, pore volume, and pore size distribution. Prior to measuring nitrogen adsorption−desorption, the produced sample was degassed at 200 °C for 4 h. Thermogravimetric analysis (TGA) was performed to determine the thermal stability of the materials using a Discovery STD-650 (TA Instruments, USA). A UV−vis spectrometer (PerkinElmer, USA) in the range of 200 to 800 nm and a photoluminescence spectrofluorometer (Shimadzu, Japan) with a 360 nm excitation wavelength were used to measure the optical characteristics. A CH instrument (Novo Control, German) was used to conduct the electrochemical analysis. A PHI 5000 (USA) was used for XPS analysis. TEM images were obtained by a transmission electron microscope (FEI, USA). The dehydrogenation of ammonia borane was studied by a gas chromatograph (Thermo Scientific, USA) with a TCD detector using a molecular sieve and argon as a carrier gas.

2.4. Photocatalytic Experiment. *2.4.1. Photocatalytic Hydrolysis of Ammonia Borane.* Dehydrogenation of NH_3BH_3 was carried out to assess the catalytic efficacy of bare Bi_2WO_6 and Ag/Bi_2WO_6 (1:1, 1:2, and 2:1) catalysts. Typically, a 10 mg Ag/Bi_2WO_6 sample was placed in a test tube with 5 mL of distilled water and Ar gas was pumped through the apparatus to render it inert. A rubber septum was used to inject 12.8 mg of NH_3BH_3 dissolved in 10 mL of water into the test tube. With continuous magnetic stirring, the reaction was carried out in the dark and under visible light irradiation. A gas chromatograph with a TCD detector and argon as a carrier gas was used to track the evolution of hydrogen.

2.5. Simulation of Surface Plasmon Resonance. The phenomenon of LSPR on Ag/Bi_2WO_6 can be easily elucidated

https://doi.org/10.1021/acsomega.2c02459
ACS Omega 2022, 7, 25466−25475

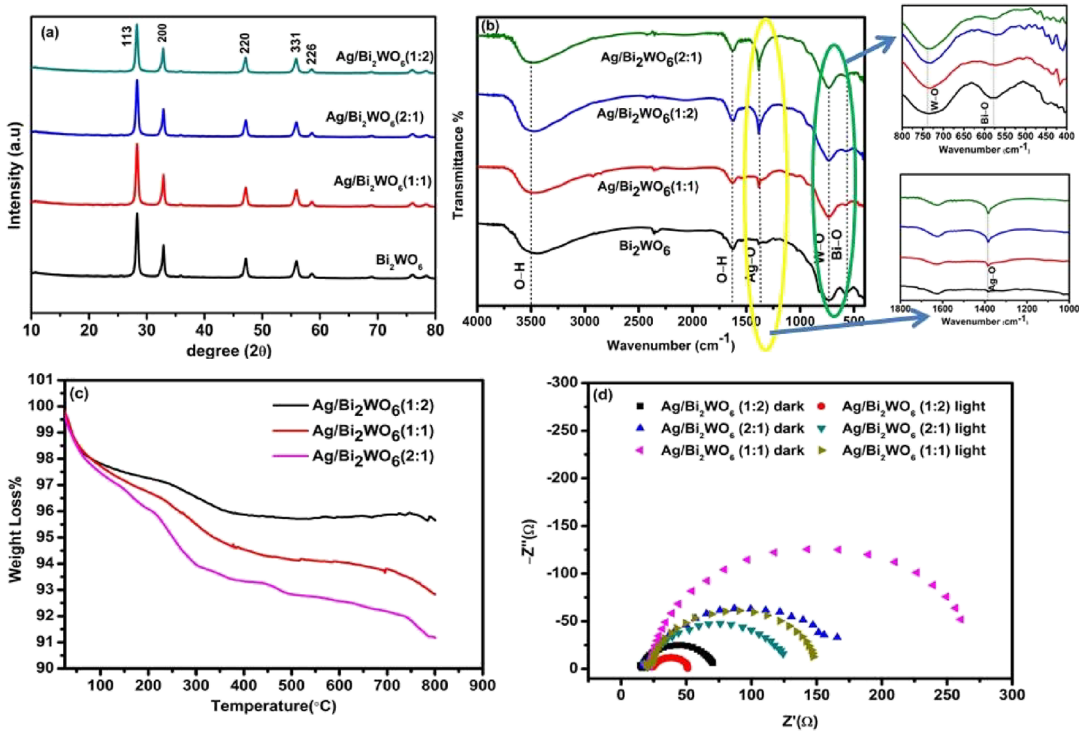

Figure 1. (a) XRD spectra, (b) FTIR spectra, (c) TGA spectra, and (d) Nyquist plot of Bi_2WO_6 and Ag/Bi_2WO_6 (1:1, 1:2, and 2:1).

by finite element method (FEM) simulation using COMSOL Multiphysics. The production of an electric field at the junction of Ag and the Bi_2WO_6 substrate was demonstrated using COMSOL modeling for a completely spherical silver particle on Bi_2WO_6 (Model-A) and a half-spherical silver particle on Bi_2WO_6 (Model-B). The geometry was created using the radius of a 12.5 nm silver nanosphere over a 50 nm × 50 nm Bi_2WO_6 substrate. The work permittivity of silver was set to −15.243 -i0.40284[31] in our simulation, while the refractive indexes of air and Bi_2WO_6 were set to 1 and 2.17, respectively.[32,33] For the simulation, a periodic boundary condition was used and the TM-polarized light wave was incident on the silver nanosphere.

3. RESULTS AND DISCUSSION

3.1. Structural Study. Figure 1a shows the diffraction peak of pure Bi_2WO_6 and Ag/Bi_2WO_6 (1:1, 1:2, and 2:1) at room temperature. Considering the orthorhombic symmetry of the material, the characteristic diffraction peaks are indexed according to JCPDS no. 73-1126.[34] There are no distinct peaks for metallic silver, which could be due to the metal's low concentration. A sharp, well-defined diffraction peak corresponds to the crystalline nature of the catalysts.

The chemical composition of the prepared Bi_2WO_6 and Ag/Bi_2WO_6 (1:1, 1:2, and 2:1) is studied using the FTIR spectra. Bi_2WO_6 has an absorption band at 500−1000 cm^{-1}. Figure 1b shows the stretching modes of Bi−O and W−O at 578.64 and 732.95 cm^{-1}, respectively.[35−37] The peaks at 3464.15 and 1624.06 cm^{-1} are ascribed to the O−H bending and stretching vibration of adsorbed H_2O molecules, respectively.[36,38] Because of the reduced amount of Ag, no separate peaks for Ag were identified, although with Ag loading, the strength of the peak at 1381.03 cm^{-1} grew, while the peak at 578.64 cm^{-1} dropped, as can be seen in the spectra. The lower intensity peak at 578.64 cm^{-1} is due to a reduction in the functional group associated with the Bi−O bonds per unit volume. Because photodeposition of Ag on Bi_2WO_6 inhibits IR radiation from reaching the molecule, light absorption by the Bi−O bond is reduced. When Ag is incorporated into Bi_2WO_6 nanoparticles, a new dip appears at 1381 cm^{-1}, which represents the Ag−O bond.[39] The position of the Bi_2WO_6 peaks did not alter after the silver coating. The peaks have not changed, showing that Ag has not harmed Bi_2WO_6's structure. Another intriguing feature of the peak at 732.95 cm^{-1}, which is connected with the stretching mode of W−O, was that it became narrower as the molar ratio of Ag loading increased. This shows that photoinduced Ag deposition on Bi_2WO_6 has altered Bi_2WO_6's reactivity in the IR region.

Figure 1c shows the TGA curve of Ag/Bi_2WO_6 (1:1, 1:2, and 2:1) in the temperature range of 25 to 800 °C. The maximum weight loss of 9% is observed in Ag/Bi_2WO_6 (2:1). The reason for weight loss is the decomposition of the silver metal; silver nanoparticles decompose and lose weight between temperatures of 200 and 450 °C.[40] The weight loss between 25 and 200 °C is due to the evaporation of moisture adsorbed from the atmosphere before performing the test. Ag/Bi_2WO_6 (1:1) has undergone a weight loss of 7%, and Ag/Bi_2WO_6 (1:2) has shown a weight loss of 4% within the given temperature range.

Electrochemical impedance spectroscopy (EIS) tests show the charge transfer mechanism in Ag/Bi_2WO_6 composites with varying molar ratios. The Nyquist plots of Ag/Bi_2WO_6 (1:1, 1:2, and 2:1) in dark and light conditions are shown in Figure 1d. The Nyquist plot's semicircle has a reduced diameter, indicating that the photogenerated electron−hole pair is effectively separated in the materials. The arc radius of Ag/Bi_2WO_6 (1:2) was substantially lower than that of Ag/Bi_2WO_6 (1:1 and 2:1) in the current EIS measurement. It shows that the LSPR effect of Ag strengthens charge transportation while

https://doi.org/10.1021/acsomega.2c02459
ACS Omega 2022, 7, 25466−25475

weakening the recombination rate, which is consistent with the photoluminescence and UV absorbance results.

FESEM images were used to examine the surface morphologies of produced Ag/Bi_2WO_6. The temperature of the hydrothermal synthesis was crucial in generating the crystalline and porous nanoflakes of the produced composite. The FESEM images of Ag/Bi_2WO_6 (1:2) are shown in Figure S3a,b. The micrograph shows several square nanoflakes with a length of about 200 nm. The nanoflakes self-assembled themselves in the form of circular colonies. Due to the relatively small sizes of silver nanoparticles, the Ag content is not visible in the images. The pores and the crystallinity of the nanoflakes were found to enhance the adsorption of the organic compound and the transfer of active species.[41,42] FESEM images of Ag/Bi_2WO_6 (1:1), Ag/Bi_2WO_6 (1:2), and Ag/Bi_2WO_6 (2:1) revealed no discernible differences. The inset spectra in Figure S3a revealed that the compound is made up of Bi, W, O, and Ag components, implying that Ag exists in Bi_2WO_6. More detailed insights into the morphology of the Ag/Bi_2WO_6 (1:1, 1:2, and 2:1) composite were investigated by TEM. The images of individual Bi_2WO_6 and the Ag/Bi_2WO_6 composite with different molar contents of Ag to Bi_2WO_6 NPs are shown in Figure 2a,b. Their selected area electron

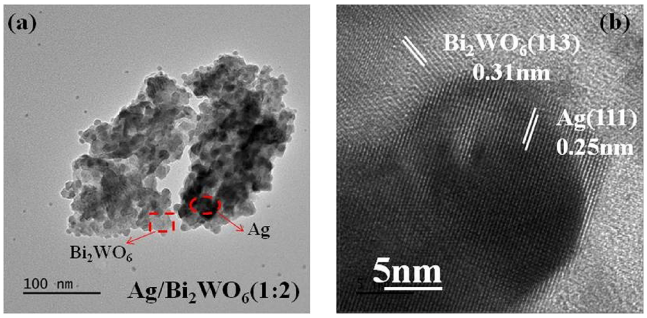

Figure 2. (a) TEM image and (b) lattice spacing of Ag/Bi_2WO_6 (1:2).

diffraction (SAED) pattern (Figure S3c) appears as bright concentric circles, which can be indexed to the (131), (200), (202), (331), and (262) planes of the Aurivillius-type layered structure Bi_2WO_6.[43] The TEM images of Bi_2WO_6 and Ag/Bi_2WO_6 with different contents of Ag loaded are similar in size. The darker region in the TEM images represents the area of Ag as it is the area of high electron density. The closer TEM image of Ag/Bi_2WO_6 (1:2) (Figure 2b) clearly shows the lattice spacing of 0.31 nm, which corresponds with the (113) lattice plane of Bi_2WO_6, and the lattice fringes of 0.25 nm match well with the (111) plane of Ag. This result further proves the successful preparation of the Ag/Bi_2WO_6 composite.[44]

The N_2 adsorption−desorption isotherm and pore size distribution of the produced photocatalysts are shown in Figure S4a,b. The Barrett−Joyner−Halenda pore size distribution plot of synthesized Bi_2WO_6 and Ag/Bi_2WO_6 (1:1, 1:2, and 2:1) exhibits a limited range of pore size distribution with average pore diameters of 15.18, 8.70, 8.69, and 8.73 nm, respectively, showing the photocatalyst's mesoporous characteristic. The specific surface area, pore width, and pore volume of Bi_2WO_6 and Ag/Bi_2WO_6 with various molar ratios of Ag to Bi_2WO_6 are shown in Table 2. There is no appreciable variation observed in the surface area of the prepared composites.

Table 2. Summary of BET Results of Pure Bi_2WO_6 and Ag/Bi_2WO_6 (1:1, 1:2, and 2:1)

catalyst	specific surface area (m^2/g)	pore diameter (nm)	pore volume (cc/g)
Bi_2WO_6	26.40	15.18	0.12
Ag/Bi_2WO_6 (1:1)	26.02	8.70	0.11
Ag/Bi_2WO_6 (1:2)	20.84	8.69	0.07
Ag/Bi_2WO_6 (2:1)	20.43	8.73	0.12

X-ray photoelectron spectroscopy (XPS) has been performed on pure Bi_2WO_6 and Ag/Bi_2WO_6 (1:1, 1:2, and 2:1). The binding energy in the spectrum is calibrated using that of C 1s (284.62 eV). Figure S5 shows the overall XPS spectrum of the Bi_2WO_6 and Ag/Bi_2WO_6 (1:1, 1:2, and 2:1) heterostructures. No peak corresponding to Ag is detected in the overall XPS spectrum of Bi_2WO_6, whereas composites of Ag/Bi_2WO_6 show Ag peaks, indicating that the photodeposition method is successful for Ag deposition. The peaks centering in the region of 159.23 and 164.57 eV (Figure 3a) can be designated to the binding energies of Bi $4f_{7/2}$ and Bi $4f_{5/2}$ in Bi^{3+}.[45] Also, the peaks centering in the region of 35.44−37.59 eV (Figure 3b) can be ascribed to W $4f_{5/2}$ and W $4f_{7/2}$ in the W^{6+} oxidation state. Ag/Bi_2WO_6 (1:2) shows the largest positive binding energy shift of 0.3 and 0.4 eV, depicting a higher oxidation state of W in the case of Ag/Bi_2WO_6 (1:2). This is due to the higher interaction of Bi_2WO_6 with Ag.[45,46] All the measured values are consistent with the previous reports.[47,48] The peaks centering at 373.74 and 367.72 eV (Figure 3c) can be ascribed to Ag $3d_{3/2}$ and Ag $3d_{5/2}$.[49] Considering the binding energies of Ag $3d_{3/2}$ and Ag $3d_{5/2}$, the valence of Ag in the heterostructure can be identified as +1.[50] The binding energy of O 1s (Figure 3d) lies at 530.20 eV, and there is a large negative shift observed in the case of the binding energy of O 1s in the Ag/Bi_2WO_6 (1:2) composite. The strong interaction of the composite with Ag creates an electric field; this weakens the bond, and O atoms in Bi_2WO_6 get replaced, creating oxygen vacancies.[45,46] The increased surface oxygen vacancy decreased the surface recombination centers and improved the charge separation efficiency, thus enhancing the photocatalytic activity.[51]

3.2. Optical Properties. A UV−vis spectrometer is used to examine the optical characteristics of the prepared plasmonic photocatalysts. In Figure 4a, the absorbance spectra of Bi_2WO_6 and Ag/Bi_2WO_6 (1:1, 1:2, and 2:1) are shown. Due to the intrinsic bandgap transition, the pure Bi_2WO_6 sample exhibits strong photoresponse qualities from UV light to visible light shorter than 430 nm, as demonstrated in the absorption spectra. The LSPR's synergistic impact with light absorption improves Ag/Bi_2WO_6 composites' absorption throughout a larger visible light area.[52,53] The photoabsorption properties of the Ag-loaded Bi_2WO_6 (1:2) composites are improved in the visible light region. The enhancement in the absorption peak may be attributed to the SPR effect.[54−56] The optical bandgaps of pure Bi_2WO_6 and Ag/Bi_2WO_6 (1:1, 1:2, and 2:1) were estimated using the tau plot and found to be 3.06, 2.71, 2.41, and 2.85 eV, respectively (Figure S6). The optical bandgap of the Ag/Bi_2WO_6 (1:2) nanophotocatalyst is calculated to be

https://doi.org/10.1021/acsomega.2c02459
ACS Omega 2022, 7, 25466−25475

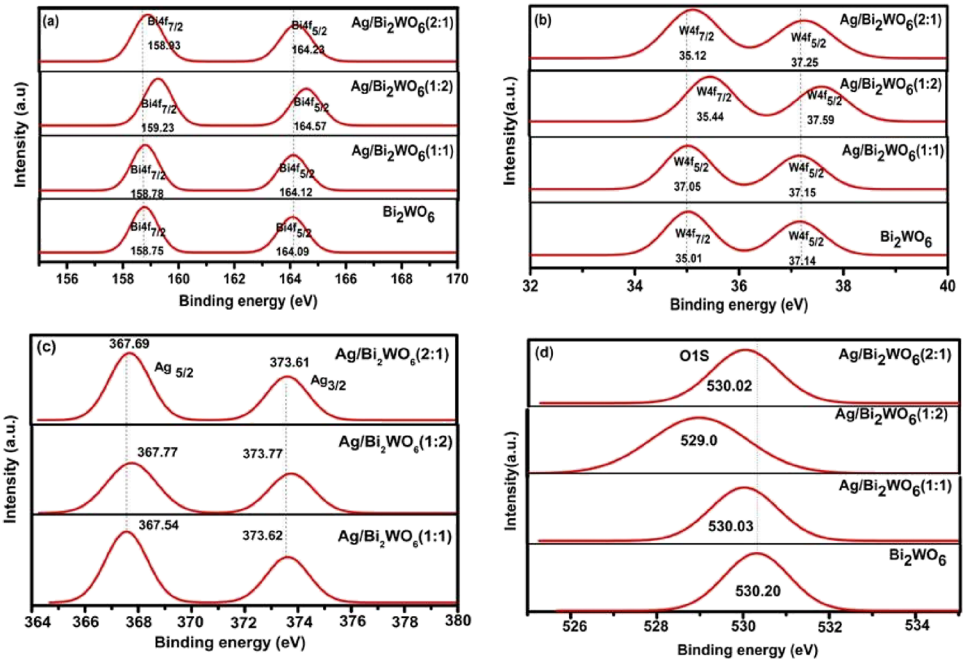

Figure 3. XPS spectra of (a) Bi 4f peaks, (b) W 4f peaks, (c) Ag 3d peaks, and (d) O 1s peaks.

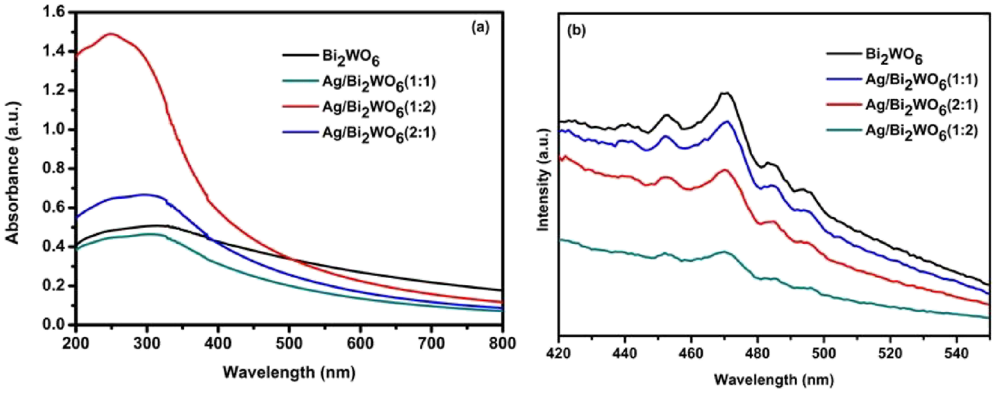

Figure 4. (a) Absorbance spectra and (b) PL spectra of pure Bi_2WO_6 and Ag/Bi_2WO_6 (1:1, 1:2, and 2:1).

2.41 eV, which is less compared to those of Bi_2WO_6 and Ag/Bi_2WO_6 (1:1 and 2:1). This result is in accordance with the XPS result, which shows that higher oxygen vacancy had been created in the Ag/Bi_2WO_6 (1:2) catalyst.

The photoluminescence (PL) emission spectra of Ag/Bi_2WO_6 can explain the electron trapping method by Ag NPs. As the Ag loading increases, the PL emission spectra in Figure 4b reveal a reduction in PL intensity. Because recombination of electron and hole pairs is a radiative process ascribed to PL emission, suppressing the recombination process diminishes the intensity of the PL spectra.[43,44] This shows that adding Ag NPs to Bi_2WO_6 can moderately limit the interaction of photogenerated holes and electrons.

3.3. SPR Effect. The real phenomenon of SPR on Ag/Bi_2WO_6 is rather complicated, but it can easily be seen in simulation. Our computation uses two models, a spherical Ag nanoparticle and hemisphere Ag nanoparticle, as shown in Figure 5a,b. Under normal irradiation of TM-polarized light (λ = 632.8 nm), the simulation result shows the creation of an electromagnetic field at the junction of Ag and Bi_2WO_6. Figure 5a indicates that spherical Ag on Bi_2WO_6 has a higher electromagnetic field enhancement than semisphere Ag on

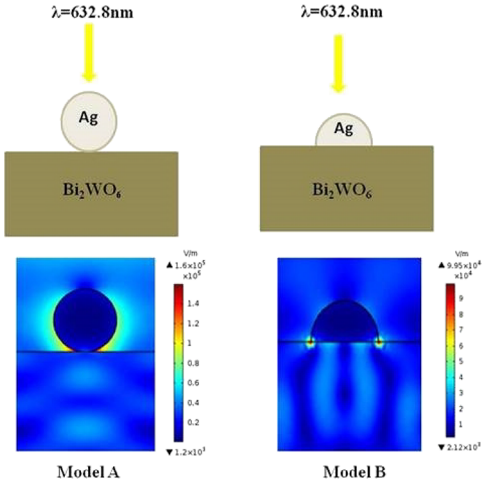

Figure 5. Electromagnetic field enhancement in spherical (model A) and semisphere (model B) Ag on Bi_2WO_6.

Bi_2WO_6 (Figure 5b). In the vicinity of plasmonic Ag, the interface in contact with the noble metal and semiconductor

https://doi.org/10.1021/acsomega.2c02459
ACS Omega 2022, 7, 25466−25475

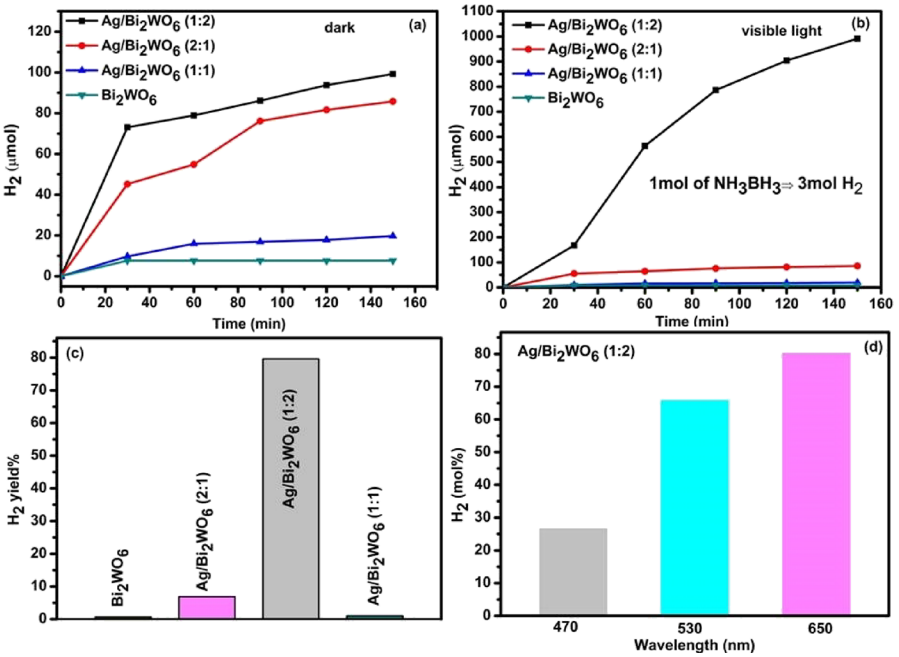

Figure 6. Plots of evolved H_2 gas as a function of reaction time from an aqueous NH_3BH_3 solution: (a) μmol of H_2 evolved within 150 min in the dark condition, (b) μmol of H_2 evolved within 150 min under visible light, (c) H_2 yield % from NH_3BH_3, and (d) wavelength dependence of initial H_2 yield rate enhancement upon LED light exposure.

thus plays a significant role in the production of an electric field. As the size of the nanoparticle increases, the distance between the "effective dipole" and its substrate image dipole increases, thereby weakening the nanoparticle and substrate interaction.[57] The contact between Ag nanospheres and the Bi_2WO_6 substrate appears to be the most important component in determining the local increased electric field according to these simulation results.[58,59]

3.4. Dehydrogenation of Ammonia Borane. Hydrogen is a clean energy source with very high energy content (120 MJ/kg). It can serve as energy in vehicular applications in the near future.[60] The low volumetric density of hydrogen makes it difficult to store. To overcome this difficulty, various storage solutions have been developed and a large number of studies have been performed on hydrogen storage materials,[61,62] such as metal hydrides[61] and organic hydrides. Solid hydrogen storage materials have gained significant attention in recent years. Ammonia borane (NH_3BH_3, AB) has drawn much attention due to its low molecular weight (30.87 g/mol) and high hydrogen capacity (19.6 wt %). AB can release hydrogen by thermal dehydrogenation, but this process requires huge power consumption and high temperature. In contrast, AB is efficient in releasing hydrogen at room temperature via dehydrogenation reaction in the presence of the catalyst under visible light irradiation.[63,64] The hydrogenation reaction of AB proceeds according to the following reaction.

$$NH_3BH_3 + H_2O \rightarrow NH_4^+ + BO_2^- + 3H_2 \quad (1)$$

According to eq 1, 1 mol of AB can produce 3 mol of H_2, which means that 12.8 mg (414 μmol) of AB could produce 1243.92 μmol of H_2. The process was carried out in a photoreactor in visible light irradiation with continuous stirring.

The hydrogenation activity of pure Bi_2WO_6 and the Ag/Bi_2WO_6 composite was investigated in the dark and also under visible light, and enhanced H_2 liberation is observed under visible light irradiation ($\lambda \approx 632$ nm). In dark conditions (Figure 6a), the Ag/Bi_2WO_6 composite exhibited catalytic efficiency with a steady-going increase in H_2 generation. The rate of the reaction exhibited by the prepared composite is very low. Pure Bi_2WO_6 exhibited a much lower reaction rate of 0.010 μmol/min, and Ag/Bi_2WO_6 (1:2) displayed 0.66 μmol/min H_2 production in 150 min. It is thus displayed that the Ag NPs and the Bi_2WO_6 composite, specifically the LSPR of Ag and W^{5+} ions, display a synergistic effect, which enables the Ag/Bi_2WO_6 hybrid to be more effective in NH_3BH_3 hydrolysis under visible light irradiation.

Pure Bi_2WO_6 produced only 0.050 μmol/min H_2 with a yield of 0.61%. The incorporation of Ag on Bi_2WO_6 facilitates enhanced visible light absorption. The composite Ag/Bi_2WO_6 (1:2) produced 6.608 μmol/min H_2 (Figure 6b) with a yield of 79.6% in 150 min (Figure 6c). However, Ag/Bi_2WO_6 (1:1) and Ag/Bi_2WO_6 (2:1) produced 0.57 and 0.13 μmol/min H_2 in 150 min, with corresponding yields of 6.9 and 1.5%, respectively. Pure Bi_2WO_6 and the Ag/Bi_2WO_6 (1:1 and 2:1) catalyst produced lower H_2. The high quantity of Ag loading in these composites might have reduced the active sites for reaction and was not appropriate to create an acceptable LSPR effect. Pure Bi_2WO_6 fails to show any LSPR effect due to the absence of Ag content, and thus, the H_2 production, in this case, is very low.

The wavelength dependence for H_2 production enhancement was also investigated by using monochromatic LEDs with wavelengths of 470, 530, and 650 nm. It was noted that the largest enhancement in H_2 production was observed in the red LED with a wavelength of 650 nm (Figure 6d). This wavelength dependence clearly elucidates that the photoactivity enhancement is due to the plasmonic effect.[65] Upon excitation by visible light irradiation, a Bi_2WO_6 support would give rise to hot energetic electrons. Subsequently, these hot electrons will be injected into the adjacent Ag NPs, allowing

https://doi.org/10.1021/acsomega.2c02459
ACS Omega 2022, 7, 25466−25475

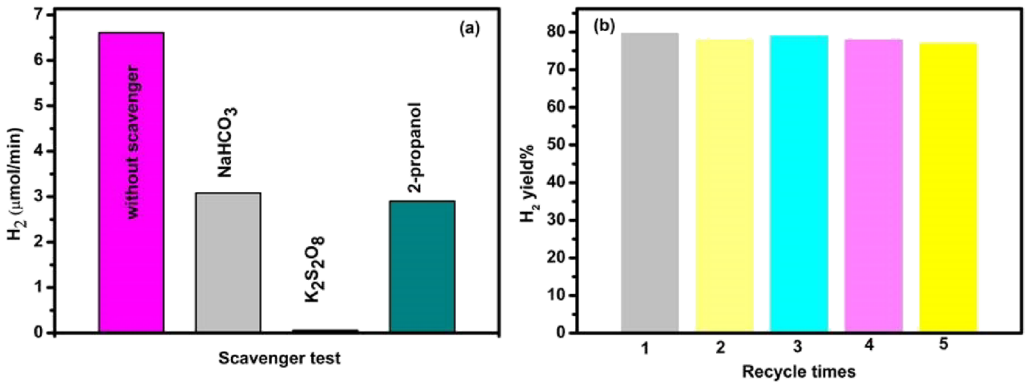

Figure 7. (a) Comparison of H_2 production activity from NH_3BH_3 solution within 150 min with or without $NaHCO_3$, $K_2S_2O_8$, and 2-propanol scavengers over plasmonic Ag/Bi_2WO_6 (1:2). (b) Five recycling experiments for NH_3BH_3 hydrolysis under visible light irradiation within 150 min.

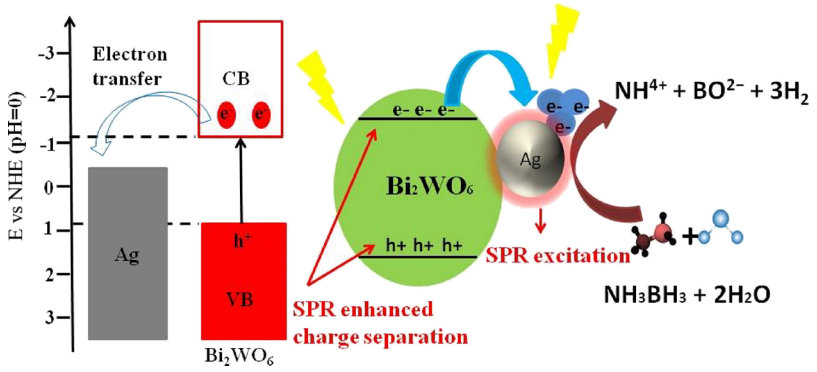

Figure 8. Band structure and electron hole process in photocatalytic hydrogen evolution for Ag/Bi_2WO_6 (1:2).

fast interfacial electron transfer. In this way, the surface Ag NPs are negatively charged and act as an electron trapper.

To understand the mechanism of photocatalytic activity of the prepared plasmonic composite, a scavenger test has been performed. $K_2S_2O_8$ as an electron scavenger, $NaHCO_3$ as a hole scavenger, and 2-propanol as a hydroxyl radical scavenger are added to the best performing photocatalyst (Ag/Bi_2WO_6 (1:2)) for the photocatalytic hydrolysis of AB under visible light irradiation in the same condition. Figure 7a shows that the H_2 yield drastically decreased from 6.608 to 0.053 μmol/min in the presence of $K_2S_2O_8$. When Ag/Bi_2WO_6 was illuminated by visible light irradiation, it produced an electron−hole pair; $K_2S_2O_8$, being a negatively charged scavenger, reacts easily with the electrons, thus resulting in activity reduction under visible light irradiation. However, hydrogenation activity decreased marginally after adding $NaHCO_3$ and 2-propanol (3.08 and 2.9 μmol/min, respectively). The scavenger tests signify that a large part of LSPR-induced hot electrons participate in the hydrogenation activity. They get excited because of the LSPR effect under visible light irradiation and generate charge pairs. Here, the negative charge acts as a main active species that directly reacts with AB to dissociate the B−N bond to form NH_3, which hydrolyzes to produce H_2 and generates an NH^{4+} ion.

The catalytic stability of the plasmonic Ag/Bi_2WO_6 (1:2) composite was investigated by recovering the photocatalyst after the reaction. The recovered photocatalyst was tested under the same condition for another five cycles. It showed considerable activity during five repeated cycles (Figure 7b). Furthermore, the XRD spectra retained the original structural property (Figure S7) even after multiple recycling experiments, which mean the efficient and stable property of plasmonic Ag/Bi_2WO_6 with high potential application prospect.

3.5. Mechanism of Photocatalytic Hydrogen Evolution. To understand the mechanism of photocatalysis with the Ag/Bi_2WO_6 heterostructure, it is desirable to interpret the synergistic effect between the constituent materials of plasmonic metal/semiconductor nanostructures, which can prove to be highly efficient to design a photocatalytic system for efficient solar energy conversion. To identify the behavior of photogenerated electrons and holes in the hybrids, we have made a band diagram of the Ag/Bi_2WO_6 hybrid based on the bandgaps and CB edge potentials of Bi_2WO_6 as well as the Fermi energy (E_F) of Ag (−0.5 V vs NHE at pH = 0) (Figure 8).[66] The CB edge potential of the Bi_2WO_6 NPs was estimated to be −1.27 V vs NHE at pH = 0 from their Mott−Schottky plot (Figure S8). Based on the band structure of the Ag/Bi_2WO_6 heterostructure, together with the results in the photocatalysis experiments, possible transfer routes for the photogenerated charge carriers could be proposed, as shown in Figure 8.

4. CONCLUSIONS

In this paper, the plasmonic nanostructures of pure Bi_2WO_6 and Ag/Bi_2WO_6 (1:1, 1:2, and 2:1) were successfully prepared by the hydrothermal and photodeposition technique. The FESEM and TEM studies show the presence of Ag nanoparticles in orthorhombic Bi_2WO_6 nanosheets. The plasmonic nanostructured Ag/Bi_2WO_6 (1:2) exhibited a localized surface plasmonic effect and presented very excellent photocatalytic activity toward dehydrogenation of NH_3BH_3 (AB), producing 6.608 μmol/min H_2 with a yield of 79.6%.

https://doi.org/10.1021/acsomega.2c02459
ACS Omega 2022, 7, 25466−25475

The combination of the noble metal with the photocatalyst introduced the plasmonic effect, which highly enhanced the photocatalytic activity of the photocatalyst. This study provides a promising strategy in exploring stable and efficient plasmonic semiconductor photocatalysts for solving hydrogen evolution problems as new energy resources and energy carriers.

■ ASSOCIATED CONTENT

Supporting Information

The Supporting Information is available free of charge at https://pubs.acs.org/doi/10.1021/acsomega.2c02459.

Charge separation mechanism, synthesis, characterization (FESEM, SAED, BET, and XPS), optical bandgap, Mott−Schottky plot of the catalyst, and XRD spectra of the used catalyst (PDF)

■ AUTHOR INFORMATION

Corresponding Author

Sanjeeb Kumar Rout − *Department of Physics, Birla Institute of Technology, Mesra, Ranchi, Jharkhand 835215, India;* orcid.org/0000-0001-5021-0805; Email: skrout@bitmesra.ac.in

Author

Shomaila Khanam − *Department of Physics, Birla Institute of Technology, Mesra, Ranchi, Jharkhand 835215, India;* orcid.org/0000-0003-2483-4723

Complete contact information is available at: https://pubs.acs.org/10.1021/acsomega.2c02459

Notes

The authors declare no competing financial interest.

■ ACKNOWLEDGMENTS

This work was financially supported by the Department of Science and Technology, Govt. of India, under the WOS-A scheme (SR/WOS-A/CS-128/2018).

■ REFERENCES

(1) Maeda, K.; Higashi, M.; Lu, D.; Abe, R.; Domen, K. Efficient Nonsacrificial Water Splitting through Two-Step Photoexcitation by Visible Light Using a Modified Oxynitride as a Hydrogen Evolution Photocatalyst. *J. Am. Chem. Soc.* **2010**, *132*, 5858−5868.

(2) Martin, D. J.; Qiu, K.; Shevlin, S. A.; Handoko, A. D.; Chen, X.; Guo, Z.; Tang, J. Angewandte Highly Efficient Photocatalytic H 2 Evolution from Water Using Visible Light and Structure-Controlled Graphitic Carbon Nitride. *Angew. Chem., Int. Ed.* **2014**, *53*, 9240−9245.

(3) Yin, Z.; Wang, Y.; Song, C.; Zheng, L.; Liu, X.; Li, S.; Lin, L.; Li, M.; Xu, Y.; Li, W.; Hu, G.; Fang, Z. Hybrid Au − Ag Nanostructures for Enhanced Plasmon-Driven Catalytic Selective Hydrogenation through Visible Light Irradiation and Surface-Enhanced Raman Scattering. *J. Am. Chem. Soc.* **2018**, *140*, 864−867.

(4) García de Abajo, F. J. Graphene nanophotonics. *Science* **2013**, *339*, 917−918.

(5) Jo, S.; Verma, P.; Kuwahara, Y.; Mori, K.; Choi, W.; Yamashita, H. Enhanced hydrogen production from ammonia borane using controlled plasmonic performance of Au nanoparticles deposited on TiO2. *J. Mater. Chem.* **2017**, *41*, 21883−22189.

(6) Fuku, K.; Hayashi, R.; Takakura, S.; Kamegawa, T.; Mori, K.; Yamashita, H. The Synthesis of Size- and Color-Controlled Silver Nanoparticles by Using Microwave Heating and Their Enhanced Catalytic Activity by Localized Surface Plasmon Resonance. *Am. Ethnol.* **2013**, *29*, 7594−7598.

(7) Tian, Y.; Tatsuma, T. Mechanisms and Applications of Plasmon-Induced Charge Separation at TiO 2 Films Loaded with Gold Nanoparticles. *J. Am. Chem. Soc.* **2005**, *127*, 7632−7637.

(8) He, C.; Shu, D.; Su, M.; Xia, D.; Abou, M.; Lin, L.; Xiong, Y. Photocatalytic Activity of Metal (Pt , Ag , and Cu) -Deposited TiO 2 Photoelectrodes for Degradation of Organic Pollutants in Aqueous Solution. *DES.* **2010**, *253*, 88−93.

(9) Qiang, Q.; Yu, J.; Cheng, B.; Ong, H. C.; Photocatalyst, P.; Hollow, A. N. Microwave-Hydrothermal Preparation and Visible light Photoactivity of Plasmonic Photocatalyst Ag-TiO2 Nanocomposites Hollow Spheres. *Chem. − Asian J.* **2010**, *5*, 1466−1474.

(10) Cheng, Z.; Zhan, X.; Wang, F.; Wang, Q.; Xu, K.; Liu, Q.; Jiang, C.; Wang, Z.; He, J. Construction of CuInS2/Ag sensitized ZnO nanowire arrays for efficient hydrogen generation. *RSC Adv.* **2015**, *5*, 81723−81727.

(11) Bajaj, G.; Soni, R. K. Applied Surface Science Nanocomposite ZnO / Au Formation by Pulsed Laser Irradiation. *Appl. Surf. Sci.* **2010**, *256*, 6399−6402.

(12) Li, J.; Cushing, S. K.; Zheng, P.; Meng, F.; Chu, D.; Wu, N. Plasmon induced photonic and energy- transfer enhancement of solar water splitting by haematitite nanorod array. *Nat. Commun.* **2013**, *4*, 1−8.

(13) Zhang, P.; Wang, T.; Gong, J. Mechanistic Understanding of the Plasmonic Enhancement for Solar Water Splitting. *Adv. Mater.* **2015**, *27*, 5328−5342.

(14) Xu, J.; Yang, W.; Huang, S.; Yin, H.; Zhang, H.; Radjenovic, P.; Yang, Z.; Tian, Z.; Li, J. CdS core-Au plasmonic nanostructure enhanced photocatalytic hydrogen evolution reaction. *Nano Energy* **2018**, *49*, 363−371.

(15) Boerigter, C.; Campana, R.; Morabito, M.; Linic, S. Evidence and Implications of Direct Charge Excitation as the Dominant Mechanism in Plasmon-Mediated Photocatalysis. *Nat. Commun.* **2016**, *7*, 1−9.

(16) Lee, J. B.; Choi, S.; Kim, J.; Nam, Y. S. Plasmonically-Assisted Nanoarchitectures for Solar Water Splitting: Obstacles and Breakthroughs. *Nano Today* **2017**, *16*, 61−81.

(17) Li, J.; Cushing, S. K.; Meng, F.; Senty, T. R.; Bristow, A. D.; Wu, N. Plasmon induced resonance energy for solar energy conversion. *Nat. Photonics* **2015**, *9*, 601−607.

(18) Long, R.; Li, Y.; Song, L.; Xiong, Y. Coupling Solar Energy into Reactions : Materials Design for Surface Plasmon-Mediated Catalysis. *Small* **2015**, *11*, 3873−3889.

(19) Zhu, C.; Meng, G.; Zheng, P.; Huang, Q.; Li, Z.; Hu, X.; Wang, X.; Huang, Z.; Li, F.; Wu, N. A Hierarchically Ordered Array of Silver-Nanorod Bundles for Surface-Enhanced Raman Scattering Detection of Phenolic Pollutants. *Adv. Mater.* **2016**, *28*, 4871−4876.

(20) Lange, H.; Jua, B. H.; Carl, A.; Richter, M.; Bastu, N. G.; Weller, H.; Thomsen, C.; von Klitzing, R.; Knorr, A. Tunable Plasmon Coupling in Distance-Controlled Gold Nanoparticles. *Langmuir* **2012**, *28*, 8862−8866.

(21) Ingram, D. B.; Christopher, P.; Bauer, J. L.; Linic, S. Predictive Model for the Design of Plasmonic Metal / Semiconductor Composite Photocatalysts. *ACS Catal.* **2011**, *1*, 1441−1447.

(22) Yu, G.; Qian, J.; Zhang, P.; Zhang, B.; Zhang, W.; Yan, W. Collective Excitation of Plasmon-Coupled Au-Nanochain Boosts Photocatalytic Hydrogen Evolution of Semiconductor. *Nat. Commun.* **2019**, *10*, 1−8.

(23) Simagina, V. I.; Komova, O. V.; Ozerova, A. M.; Netskina, O. V.; Odegova, G. V.; Kayl, N. L.; Filippov, T. N. TiO 2 -Based Photocatalysts for Controllable Hydrogen Evolution from Ammonia Borane. *Catal. Today* **2021**, *379*, 149−158.

(24) Zhang, M.; Xiao, X.; Wu, Y.; An, Y.; Xu, L.; Wan, C. Hydrogen Production from Ammonia Borane over PtNi Alloy Nanoparticles Immobilized on Graphite. *Catalysts* **2009**, *9*, 1009.

(25) Qi, X.; Li, X.; Chen, B.; Lu, H.; Wang, L.; He, G. Highly Active Nanoreactors: Patchlike or Thick Ni Coating on Pt Nanoparticles Based on Con Fi Ned Catalysis. *ACS Appl. Mater. Interfaces* **2016**, *8*, 1922−1928.

(26) Mori, K.; Miyawaki, K.; Yamashita, H. Ru and Ru-Ni Nanoparticles on TiO Support as Extremely Active Catalysts for Hydrogen Production from Ammonia Borane Ru and Ru-Ni Nanoparticles on TiO 2 Support as Extremely Active Catalysts for Hydrogen Production from Ammonia Borane. *ACS Catal.* **2016**, *8*, 3128−3135.
(27) Yin, H.; Kuwahara, Y.; Mori, K.; Cheng, H.; Wen, M.; Huo, Y.; Yamashita, H. Localized Surface Plasmon Resonances in Plasmonic Molybdenum Tungsten Oxide Hybrid for Visible-Light-Enhanced Catalytic Reaction. *J. Phys. Chem. C* **2017**, *121*, 23531−23540.
(28) Yousef, A.; Barakat, N. A. M.; El-newehy, M. H.; Ahmed, M. M.; Kim, H. Y. Catalytic hydrolysis of ammonia borane for hydrogen generation using Cu (0) nanoparticles supported on TiO2 nanofibers. *Colloids Surf., A* **2015**, *470*, 194−201.
(29) Meng-yu, X.; Kang-yang, S.; Xin-yuan, P.; Ren-jang, W.; Murthy, C.; Wei-chen, C. Hydrogen Production by Photocatalytic Water-Splitting on Pt-Doped TiO2-ZnO under Visible Light. *J. Taiwan Inst. Chem. Eng.* **2017**, *71*, 426−432.
(30) Pant, B.; Raj, H.; Park, M.; Liu, Y.; Choi, J.; Barakat, N. A. M.; Kim, H. Electrospun CdS − TiO 2 Doped Carbon Nano Fi Bers for Visible-Light-Induced Photocatalytic Hydrolysis of Ammonia Borane. *Catal. Commun.* **2014**, *50*, 63−68.
(31) Jhonson, P. B.; Christy, R. W. Optical constants of the noble metal. *Phys. Rev.* **1972**, *6*, 4370.
(32) Cheng, C.; Cheng, C. Refractive Index Measurement by Prism Autocollimation. *Am. J. Phys.* **2014**, *82*, 214−216.
(33) Mahanty, S.; Ghose, J. Preparation and Optical Studies of Polycrystalline Bi2W06. *Mater. Lett.* **1991**, *11*, 254−256.
(34) Hubbard, C. R.; Mighell, A. D. JCPDS-ICDD Research Associateship (Cooperative Program with NBS/NIST). *J. Res. Natl. Inst. Stand. Technol.* **2001**, *106*, 1013−1028.
(35) Khanam, S. Decolourization of Rhodamine B and Methylene Blue Dyes in the Presence of Bismuth Tungstates : A Detailed Investigation on the Effect of Grain Size. *Bull. Mater. Sci.* **2021**, *44*, 1−7.
(36) Wan, J.; Xue, P.; Wang, R.; Liu, L.; Liu, E.; Bai, X.; Fan, J.; Hu, X. Applied Surface Science Synergistic Effects in Simultaneous Photocatalytic Removal of Cr (VI) and Tetracycline Hydrochloride by Z-Scheme Co 3 O 4 / Ag / Bi 2 WO 6 Heterojunction. *Appl. Surf. Sci.* **2019**, *483*, 677−687.
(37) Mcdowell, N. A.; Knight, K. S.; Lightfoot, P. Unusual High-Temperature Structural Behaviour in Ferroelectric Bi 2 WO 6. *Chem. − Eur. J.* **2006**, *12*, 1493−1499.
(38) Chem, J. M.; Wang, D.; Xue, G.; Zhen, Y.; Li, D. Monodispersed Ag Nanoparticles Loaded on the Surface of Spherical Bi 2 WO 6 Nanoarchitectures with Enhanced Photocatalytic Activities. *J. Mater. Chem.* **2012**, *22*, 4751−4758.
(39) Sayadi, M. H.; Ahmadpour, N.; Homaeigohar, S. Photocatalytic and Antibacterial Properties Of Ag CuFe2O4@WO3 magnetic nanocomposite. *Nanomaterials* **2021**, *11*, 298.
(40) Adebayo-tayo, B.; Salaam, A.; Ajibade, A. Heliyon Green Synthesis of Silver Nanoparticle Using Oscillatoria Sp . Extract , Its Antibacterial , Antibio Fi Lm Potential and Cytotoxicity Activity. *Heliyon* **2019**, *5*, No. e02502.
(41) Zhang, L.; Wang, W.; Chen, Z.; Zhou, L.; Zhu, W. Fabrication of Flower-like Bi 2 WO 6 Superstructures as High Performance Visible-Light Driven Photocatalysts. *J. Mater. Chem.* **2007**, *17*, 2526−2532.
(42) Wu, Q.; Cui, Y.; Yang, L.; Zhang, G.; Gao, D. Facile In-Situ Photocatalysis of Ag / Bi 2 WO 6 Heterostructure with Obviously Enhanced Performance. *Sep. Purif. Technol.* **2015**, *142*, 168−175.
(43) Shen, J.; Xue, J.; Chen, Z.; Ni, J.; Tang, B.; He, G.; Chen, H. One-Step Hydrothermal Synthesis of Peony-like Ag / Bi 2 WO 6 as Efficient Visible Light-Driven Photocatalyst toward Organic Pollutants Degradation. *J. Mater. Sci.* **2018**, *53*, 4848−4860.
(44) Shen, J.; Xue, J.; He, G.; Ni, J.; Tang, B. Construction of 3D Marigold-like Bi 2 WO 6 / Ag 2 O / CQDs Heterostructure with Superior Visible-Light Active Photocatalytic Activity toward Tetracycline Degradation and Selective Oxidation. *J. Mater. Sci.* **2018**, *53*, 12040−12055.
(45) Di, J.; Xia, J.; Ge, Y.; Li, H.; Ji, H.; Xu, H.; Zhang, Q.; Li, H.; Li, M. Novel visible-light driven hybrid material with enhanced photocatalytic activity CQDs/Bi2WO6 toward organic pollutants degradation and mechanism inside. *Appl. Catal., B* **2015**, *168*, 51−61.
(46) Tian, J.; Sang, Y.; Yu, G.; Jiang, H.; Mu, X.; Liu, H. A Bi 2 WO 6 -Based Hybrid Photocatalyst with Broad Spectrum Photocatalytic Properties under UV , Visible , and Near-Infrared Irradiation. *Adv. Mater.* **2013**, *25*, 5075−5080.
(47) Jonjana, S.; Phuruangrat, A.; Thongtem, S.; Thongtem, T. Preparation and enhanced photo catalytic performance of AgCl/Bi2MoO6 heterojunction. *Mater. Lett.* **2016**, *179*, 162−165.
(48) Phuruangrat, A.; Dumrongrojthanath, P.; Thongtem, S.; Thongtem, T. Hydrothermal Synthesis of I-Doped Bi2WO6 for Using as a Visible-Light-Driven Photocatalyst. *Mater. Lett.* **2018**, *224*, 67−70.
(49) Phuruangrat, A.; Siri, S.; Wadbu, P.; Thongtem, S.; Thongtem, T. Microwave-Assisted Synthesis, Photocatalysis and Antibacterial Activity of Ag Nanoparticles Supported on ZnO Flowers. *J. Phys. Chem. Solids* **2019**, *126*, 170−177.
(50) Yu, A.; Dovnar, R. I.; Id, A. V. N. Plasmon Resonance of Silver Nanoparticles as a Method of Increasing Their Antibacterial Action. *Antibiotics* **2018**, *7*, 80.
(51) Qian, H. J.; Wu, D.; Wang, P.; Ao, Y.; Hou, J.; Qian, J. Effect of oxygen vacancy on enhanced photocatalytic activity of reduced ZnO nanorod arrays. *Appl. Surf. Sci.* **2015**, *325*, 112−116.
(52) Li, B.; Tan, L.; Liu, X.; Li, Z.; Cui, Z.; Liang, Y.; Zhu, S.; Yang, X.; Kwok Yeung, K. W.; Wu, S. Superimposed Surface Plasma Resonance Effect Enhanced the Near-Infrared Photocatalytic Activity of Au @ Bi 2 WO 6 Coating for Rapid Bacterial Killing. *J. Hazard. Mater.* **2019**, *380*, No. 120818.
(53) Lu, C.; Li, X.; Wu, Q.; Li, J.; Wen, L.; Dai, Y.; Huang, B.; Li, B.; Lou, Z. Constructing Surface Plasmon Resonance on Bi 2 WO 6 to Boost High-Selective CO 2 Reduction for Methane. *ACS Nano* **2021**, *15*, 3529−3539.
(54) Jia, J.; Du, X.; Liu, E.; Wan, J.; Pan, C.; Ma, Y.; Hu, X.; Fan, J. Highly Efficient and Stable Au / Bi 2 MoO 6 / Bi 2 WO 6 Heterostructure with Enhanced Photocatalytic Activity for NO Gas Removal under Visible Light Irradiation. *J. Phys. D: Appl. Phys.* **2017**, *50*, 145103.
(55) Chen, J.; Shen, S.; Guo, P.; Wang, M.; Su, J.; Zhao, D.; Guo, L. Plasmonic Ag@SiO2 core/shell structure modified g-C3N4 enhanced visible light photocatalytic activity. *J. Mater. Res.* **2014**, *29*, 64−70.
(56) Yu, L.; Ye, Z.; Li, J.; Ma, C.; Ma, C.; Liu, X.; Wang, H.; Tang, L.; Huo, P.; Yan, Y. Photocatalytic Degradation Mechanism of Tetracycline by Ag @ ZnO / C Core − Shell Plasmonic Photocatalyst Under Visible Light. *NANO* **2018**, *13*, 1850065.
(57) Albella, P.; Garcia-cueto, B.; Gonz, F.; Moreno, F.; Wu, P. C.; Kim, T.; Brown, A.; Yang, Y.; Everitt, H. O.; Videen, G. Shape Matters : Plasmonic Nanoparticle Shape Enhances Interaction. *Nano Lett.* **2011**, *9*, 3531−3537.
(58) Yao, G.; Liu, Q.; Zhao, Z. Studied localized surface plasmon resonance effects of Au nanoparticles on TiO2 by FDTD simulation. *Catalysts* **2018**, *8*, 236.
(59) Yu, Z.; Sang, L.; Chen, Y. Applied Surface Science A Novel Route to Visualize the Hot Electron Transfer Process in Ag @ SiO 2 -TiO 2 for Solar-Hydrogen Conversion. *Appl. Surf. Sci.* **2020**, *527*, No. 146772.
(60) Schlapbach, L.; Züttel, A. Hydrogen storage material for mobile applications. *Materials for sustainable energy: a collection of peer-reviewed research and review articles from nature publishing group.* **2011**, 265−270.
(61) Chen, P.; Xiong, Z.; Luo, J.; Lin, J.; Tan, K. L. Interaction of Hydrogen with Metal Nitrides and Imides. *Nature* **2002**, *420*, 302−304.
(62) Singh, S. K.; Zhang, X.; Xu, Q. Room-temperature hydrogen generation from hydrous hydrazine for chemical hydrogen storage. *J. Am. Chem. Soc.* **2009**, *131*, 9894−9895.

https://doi.org/10.1021/acsomega.2c02459
ACS Omega 2022, 7, 25466−25475

(63) Lu, Z.; Xu, Q. Recent progress in boron-and nitrogen-based chemical hydrogen storage. *Funct. Mater. Lett.* **2012**, *05*, 1230001.
(64) Hu, T.; Ku, M. F.; Lentz, D. Hydrazine Borane : A Promising Hydrogen Storage Material. *J. Am. Chem. Soc.* **2009**, *131*, 7444−7446.
(65) Yin, H.; Kuwahara, Y.; Mori, K.; Yamashita, H. Plasmonic metal MoxW1-xO3-y for visible-light enhanced hydrogen production from ammonia borane. *J. Mater. Chem. A* **2018**, *6*, 10932−10938.
(66) Li, H.; Yu, H.; Quan, X.; Chen, S.; Zhang, Y. Uncovering the Key Role of Fermi Level of Electron Mediator in Z-Scheme Photocatalyst by Detecting Charge Transfer Process of WO 3 -Metal-GC 3 N 4 (Metal = Cu , Ag , Au). *ACS Appl. Mater. Interfaces* **2016**, *8*, 2111−2119.

https://doi.org/10.1021/acsomega.2c02459
ACS Omega 2022, 7, 25466−25475